RSC Advances

ROYAL SOCIETY OF CHEMISTRY

www.rsc.org/advances

Investigating the mechanism of phase transformations and migration in olivine at high temperature

R. Michel[1*], M. R. Ammar[1], E. Veron[1], P. Simon[1], J. Poirier[1]*

[1]CNRS, CEMHTI UPR3079, Univ. Orléans, F-45071 Orléans, France

*Corresponding author at: CEMHTI-CNRS UPR3079/Université d'Orléans
tel: +33 (0) 238 25 55 14; fax: +33 (0) 238 63 81 03
E-mail address: rudy.michel@cnrs-orleans.fr and jacques.poirier@univ-orleans.fr

Abstract

A framework is presented to define the formation and migration mechanisms of oxides in olivine during their phase transformations at high temperature. Therefore, the behaviour of olivine particles has been investigated at 1400°C at two different residence times: 4h and 115h. The structural and vibrational properties of the resulting materials were analysed using both X-ray diffraction (notably, *in situ* X-ray diffraction) and Raman spectroscopy including its mapping mode. The measurements have shown the migration of magnetite and enstatite from the inner part of olivine particles toward the surface, which results in the alteration of the solid solution and the intergranular reaction of particles. These results contribute to a better knowledge of olivine material science in particular, catalysis, refractory and engineering areas.

Keywords: Olivine, Magnetite, Phase transformation, Raman, HT-XRD, Intergranular reaction

1. Introduction

Olivine is an abundant raw material widely used in various domains, owing to its chemical and physical properties that make it an excellent material for different applications such as refractories [1] catalysts [2,3], as well as engineering materials [4–6]. Olivine is an orthosilicate originating from the upper part of the earth mantle [7]. Its orthorhombic structure consists of isolated SiO_4^{4-} tetrahedra, each of them being shared by three octahedral cations Mg^{2+} and Fe^{2+} [8]. The general formula of olivine is $(Mg_{1-x}Fe_x)_2SiO_4$, which is a continuous solid solution between forsterite Mg_2SiO_4 and fayalite Fe_2SiO_4. By contrast, olivine undergoes phase transformations upon temperature and hence conducts to the alteration of the solid solution. It is therefore important to get a thorough understanding of the various structural modifications.
An extensive literature is available on the property enhancement of olivine, for example, calcination treatment [3,9], metal doping [2,10–13], and the introduction of additives [14–16]. Although the formation of the constituents such as iron oxides is confirmed, their nature and mechanism are not well defined.
The present paper reports on the mechanism describing the formation of oxides through the host matrix at high temperature and study the reactivity of olivine particles. In order to investigate the behavior of the material, X-ray diffraction was used to probe the crystalline phases. This technique is improved by an *in situ* method. The phase migration of the formed oxides in olivine particles as well as their intergranular reaction, due to the thermal treatment, is clearly highlighted by using optical microscopy and Raman spectroscopy analysis.

2. Material and characterisations

In the current investigation, the trials were conducted on olivine particles calcined at 1400°C and two different residence times (4h and 115h) under air in an open-air atmosphere furnace. This temperature has frequently been used in chemical engineering [3,17] allowing also the intergranular reaction of the material [18,19].

The investigated material was a standard olivine mined at the Åheim Plant in Norway and provided by SIBELCO company. This material was previously used in our recent work [20] and was formulated as $(Mg_{0.92}Fe_{0.08})_2SiO_4$. Olivine was sieved to obtain particle sizes ranging from 400 to 500 µm.
After calcination, a part of the samples was suitably crushed, prior to be characterised by X-ray diffraction. The rest of the samples was embedded in a resin then, polished, for the purpose of having a mirror surface suitable for observation by optical microscopy and vibrational characterisation by Raman spectroscopy.

The crystalline phases were determined by powder X-ray diffraction (XRD), performed on a Bruker D8 Advance diffractometer (Cu $K_{\alpha1,2}$ radiation, 40 kV, and 30 mA) equipped with a linear Vantec detector. Every scan was recorded on a 2θ ranging from 10 to 80° with a step size of 0.016° and 10s/step.
To highlight the different steps leading to the appearance of the various phases, olivine powder was also analysed by *in situ* X-ray diffraction as a function of the heat-treatment temperature (HT-XRD). The apparatus was operated under air. The sample was installed on a platinum ribbon heating stage and the data were collected using a HTK16 Anton Paar chamber.

The optical quality of the sample cross-sections was first investigated by visual examination, and then by optical microscopy. The snapshots were qualitatively collected in both bright field and dark field modes.
Then, the phase analyses of the samples, at the micrometer scale, were performed by Raman spectroscopy. The spectra were recorded on an InVia Reflex Renishaw spectrometer. A laser beam (633nm wavelength and 13mW output power), was focused onto the sample, through a x100 microscope objective. The Raman-scattered light was collected by a holographic grating of 1800 grooves/mm and detected by a Charge Coupled Device (CCD) camera.
In order to get a complete picture of the migration of various phases between and/or within the particles, Raman mapping has been performed. In this particular case, a holographic grating of 600 grooves/mm and two independent objectives (x20 and x100) were used. The data were processed by principal component analysis (PCA) giving an indication of independent components in the map. Then, a Direct Classical Least squares (DCLS) method was used consisting in the rigorously map reconstruction by a linear combination of spectra from the pure components contained in the sample.

3. Results and discussions

The data obtained in a previous study indicate that olivine forms hematite and magnetite phases at high temperature [20]. In the present study, the interaction between olivine particles is particularly investigated as a function of the heat-treatment temperature in order to understand the mechanism of reactivity. First, the evolution of olivine at high temperature is studied by both *ex situ*, and *in situ* XRD.
Figure 1 shows diffractograms collected at ambient temperature, of the natural olivine sample, and those calcined at 1400°C for 4h and 115h.

$(Mg_{1.81}Fe_{0.19})SiO_4$ (JCPDS 01-088-0998) is identified as the main phase of the natural olivine (Fig.1a). Once the material is subjected to high temperatures, the main phase turns into forsterite (Mg_2SiO_4, JCPDS 01-080-0944), as observed on the diffractograms of figure 1b and 1c. The second major phase of natural olivine (Fig.1a) is enstatite ($MgSiO_3$, JCPDS 00-019-0768) mainly observed at $2\theta = 28.1°$ and 31°. Moreover, the clino-enstatite phase (JCPDS 00-019-0769), which is observed on the natural olivine diffractogram (Fig.1a), turns into proto-enstatite (JCPDS 01-074-0816) at high temperature (Fig.1b and Fig.1c), and this polymorphic phase increases at 1400°C from 4h to 115h as illustrated in the insert of figure 1.
The natural olivine (Fig.1a) also exhibits a serpentine phase which completely disappears at high temperature. Note that serpentine is a hydrated magnesium silicate formulated as $(Mg_3Si_2O_5(OH)_4)$. This phase gathers together antigorite, chrysotile and lizardite phases.
On the other hand, figure 1b and 1c clearly show the appearance of a spinel phase which is attributed to magnetite (Fe_3O_4, JCPDS 01-071-6336).

Figure 2 (top part) displays 3D *in situ* XRD analyses of olivine samples in the 2θ range from 22 to 34°, which provides an overall picture of different phases occurring at varying temperatures. Five selected diffractograms are extracted in the 2θ range from 15 to 45° at 50°C, 550°C, 1050°C, 1225°C and 1400°C as shown in figure 2 (bottom part).
The first observations show the dehydration of serpentine which continues to be observed on the *in situ* diffractograms up to 550°C while enstatite phase is highly present from ambient temperature up to 1320°C with the formation of proto-enstatite from 1200°C.
Moreover, a new phase appears between 725°C and 1150°C which was identified as hematite α -Fe_2O_3 (see its corresponding diffractogram recorded at 1050°C on Fig.2c). The disappearance of the hematite phase was accompanied by the appearance of another iron oxide called magnetite which is highly present between 1150 and 1320°C (its corresponding diffractogram recorded at 1225°C is shown on Fig.2d). Above 1320°C, enstatite and magnetite are present in liquid state and do not appear anymore on the diffractograms, only forsterite reflections remain.
The oxidation of magnetite into hematite and the reduction of hematite into magnetite are known. However, Michel et al have shown the thermodynamic phase diagram of Fe_2SiO_4–O_2 and indicates that both magnetite and hematite phases are present at 1400°C under air (log $p(O_2) = -0.70$) and only magnetite is present above 1400°C [20].

There are obviously some differences between ex situ and in situ diffractograms owing simply to the sample preparation. For in situ XRD analysis, natural olivine powder was used, while the calcined particles were first crushed prior to be analysed by ex situ method. Consequently the oxidation degree is not necessarily the same for both methods.
Since olivine material has been calcined under air, the resulting chemical transformations, owing to the temperature increase, can be described as follows: at first, serpentine is completely dehydrated at 550°C according to reaction (1) forming forsterite and enstatite phases. Then, when olivine $(Mg_{1.81}Fe_{0.19})SiO_4$ reacts with oxygen, fayalite (Fe_2SiO_4 from solid solution of natural olivine) can produce hematite and silica at around 725°C according to reaction (2). Consequently, the formation of silica induces an increase in the amount of enstatite according to reaction (3). Finally, hematite decreases and magnetite increases above 1150°C. The evidence suggests that hematite is reduced into magnetite according to reaction (4). For the Gibbs free energy, the reaction module of Factsage™ software was used. The energies of reactions (1-3) show their spontaneity. The reaction (4) is not thermodynamically spontaneous. The presence of magnetite can be explained by a catalytic reaction.

$$2Mg_3Si_2O_5(OH)_4 \rightarrow 2Mg_2SiO_4 + 2MgSiO_3 + 4H_2O \qquad \Delta G°_{550} = -193.3\ kJ \quad (1)$$

$2Fe_2SiO_4 + O_2 \rightarrow 2Fe_2O_3 + 2SiO_2$ $\Delta G°_{725} = -275$ kJ (2)

$Mg_2SiO_4 + SiO_2 \rightarrow 2MgSiO_3$ $\Delta G°_{725} = -1.9$ kJ (3)

$3Fe_2O_3 \rightarrow 2Fe_3O_4 + {}^1/_2O_2$ $\Delta G°_{1150} = 49.5$ kJ (4)

Although the significant decrease of hematite reflections below the detection limit on XRD diffractogram at high temperatures, suggesting its possible complete transformation into magnetite, Michel et al. have shown by Raman spectroscopy the coexistence of hematite and magnetite phases in olivine subjected to 1400°C and the spatial distribution of these phases was completely heterogeneous [20]. In fact, numerous experiments have established the stabilization of iron oxide in a silica matrix. According to Tadic et al. [21], a silica matrix can allow stabilisation of hematite by some encapsulation phenomenon. Chen et al. [22] have shown this effect with maghemite and Morel et al. with magnetite [23]. Mostly, iron oxide encapsulated by silica is performed in an aqueous solution [22,23] or by sol-gel process [21].

Figures 3 provides two optical micrographs of calcined olivine grains at 1400°C for 4h, obtained from reflected light using bright field (BF) and dark field (DF) modes respectively.
Within the analysed area, several features were highlighted by using Raman spectroscopy. Figures 3a and 3b display Raman spectra obtained at two distinct positions. The presence of the doublet, located at 822 and 855 cm^{-1}, is characteristic of forsterite phase and arises from a mixture of symmetric and anti-symmetric internal stretching vibrational modes (A_g symmetry) of the SiO_4^{4-} ions. However, the intensity ratio of the two A_g modes exhibits distinct values from the two analysed positions. It is worthy to note that the scattering Raman intensity is expected to vary by orders of magnitude depending, notably on the orientation of the crystal. This clearly means that the intergranular reaction occurs between distinct particles represented by the regions delimited by the dashed lines in figure 3 (DF).

Figures 3c and 3d display two Raman spectra showing similar symmetry assignments (A_{1g}, T_{2g} and E_g symmetries [24]) except that the relative intensities as well as the Raman bandwidths are distinctly different. These Raman spectra are related to Fe_3O_4 crystals (magnetite).
Basically, this material crystallises, at ambient pressure and temperature, in the cubic inverse spinel structure (Fig.3d) and belongs to Fd3m space group [25,26].
Literature describes two magnetite structures as direct spinel ($[Fe^{2+}]_A[Fe^{3+} + Fe^{3+}]_BO_4$) and inverse spinel ($[Fe^{3+}]_A[Fe^{2+} + Fe^{3+}]_BO_4$). Two different kinds of cation sites exist in the magnetite inverse spinel structure: tetrahedrally (A) coordinated sites occupied by Fe^{3+} and octahedrally (B) coordinated sites occupied by a random distribution of Fe^{3+} and Fe^{2+} [27].
The decreasing of the A_{1g} mode and its broadening may possibly be explained by the electron exchange (hopping) between Fe^{2+} (B) and Fe^{3+} (A) cations. This result suggests that the corresponding Raman spectrum, observed on Fig.3c, describes a direct spinel structure. Generally, such kinds of transition states (inverse-direct spinel) occurs under particular conditions. Ovsyannikov et al. have shown a sluggish valence transition for magnetite from the inverse state to the normal (direct) one at room temperature and under high pressure [28]. Note that in our experimental conditions, direct spinel is formed at atmospheric pressure and high temperature (1400°C).
Additionally, other features are also detected by Raman spectroscopy in the analysed area, such as the occurrence of enstatite and hematite as illustrated in figures 3e and 3f, despite the fact that the amount of the latter phase is supposed to be too low to be detected by XRD above 1150°C.

Raman mapping is a powerful tool for probing the distribution of the different phases described above. Owing to the huge number of the collected spectra, a first data processing by Principal Component Analysis (PCA) was performed giving an indication of the various components that are present in the Raman spectra. The reconstruction of the maps has been achieved using a Direct Classical Least Squares (DCLS) method which is based on a linear combination of the spectra from the various pure components obtained by PCA. Figure 4 presents the reflected light micrograph obtained by bright field mode on the calcined olivine grains at 1400°C for 4h and the map scores showing the spatial distribution of each of five constituents [(a) forsterite, (b) enstatite, (c) hematite, (d) magnetite (direct spinel), and (e) magnetite (inverse spinel)] located in the region defined by a rectangle in the optical micrograph. As previously mentionned, Raman spectra performed on olivine have shown (Fig.3d) that olivine particles are characterised by different crystal orientations. Raman mapping of forsterite (Fig.4a) confirms the fact that three particles of olivine react at high temperature. These particles seem to have a low content of hematite (Fig.4c). However, enstatite appears to be mainly located in the intergranular area (Fig.4b). Inverse spinel is found inside and between olivine particles while direct spinel is located at the interface between forsterite and enstatite phases (Fig.4d and 4e).

Similarly to Fig. 4 but for a longer annealing time, figure 5 exhibits the reflected light micrograph obtained by bright field mode on the calcined olivine grains at 1400°C, during 115h and the Raman map scores of only four constituents [(a) forsterite, (b) enstatite, (c) direct spinel, and (d) inverse spine].

The reaction is performed on three olivine particles. Contrary to the calcination during 4h, no hematite signature has been detected after relatively long calcination time of 115h and presents a nearly total transformation into magnetite. The latter is only present in the intergranular area with enstatite (Fig.5b, 5c, 5d), and the particles are exclusively composed of forsterite (Mg_2SiO_4) (Fig.5a). Direct spinel appears to be bordered by enstatite and inverse spinel.

Eventually, Raman maps show that raw olivine $(Mg_{0.92}Fe_{0.08})_2SiO_4$ present a natural formation of magnetite spinels encapsulated in silica matrix (enstatite $MgSiO_3$) at high temperature. Moreover, inside olivine particles, Mg_2SiO_4, Fe_2O_3, Fe_3O_4 and $MgSiO_3$ are formed and the latter two components migrate in the particle to the surface and generate consequently an intergranular reaction. As far as olivine alteration is concerned, Gay et al. [29] have shown the formation of a particular phase, the so-called “iddingsite”. This phase is described as dark red brown to reddish-brown and there are few literatures about its composition (MgO, SiO_2, Fe_3O_4 or Fe_2O_3 and H_2O) [29]. Although, iddingsite can be produced at low temperature, High Temperature Iddingsite (HTI) presents more interest in our conditions of high temperature (1400°C). This so-called "Iddingsitisation" is a continuous transformation into the solid state, during which the original olivine crystal may pass through various stages of structural and chemical changes.

Clement et al [30] have studied iddingsite formation in volcanoes and present HTI as a product of olivine alteration at temperatures higher than 1075°C in a process occurring before emplacement of the lava (either in the chimney or in the magma chamber), as a result of a temporary increase in oxygen fugacity and H_2O content.

It could be concluded that, in the present study, olivine forms iddingsite phase at high temperature. This phase is composed of enstatite and magnetite spinel, allowing the intergranular reaction between olivine particles.

According to all the results obtained by XRD and Raman spectroscopy, a mechanism is proposed here to describe the phase transformations and the component migration occurring in olivine at high temperature.
As illustrated in figure 6, the mechanism involved is divided into 4 stages.

- Stage 1: olivine is dehydrated at 550°C
- Stage 2: olivine reacts with oxygen. Hematite is formed between 725°C and 1150°C.
- Stage 3: hematite is reduced into magnetite spinel above 1150°C. Olivine particles are mainly composed of forsterite with low amounts of enstatite, hematite and magnetite. However, veins of inverse spinel can be formed and inverse spinel is found around the particles [20].
- Stage 4: At 1400°C, the particles react and the grain boundary interphases are composed of iddingsite (magnetite and enstatite). These particles are mainly composed of forsterite.

Conclusion

Despite the fact that prior works have documented the characterisation of olivine used for different physical and chemical applications, numerous studies have not yet shown the mechanism of olivine evolution at high temperature. In the present study, the behaviour of olivine at high temperature is described and the mechanism involved is proposed to show the oxides evolution within the particles and the migration of magnetite spinels and enstatite. The *in situ* XRD and Raman spectroscopy appear to be powerful techniques to identify and determine the phase transformations that occur when olivine is subjected to high temperatures. We found that the material forms magnetite spinel and enstatite after calcination which spread from the inner part of the particles toward the surface, eventually leading to the particle intergranular reaction. These findings offer an understanding of olivine behaviour and confirm the formation of magnetite. In addition, the reactive phase is iddingsite and present enstatite, magnetite spinel under inverse and direct structure. Our results provide evidence of the nature of the phase transformations and contribute to a better knowledge of the reactivity and mechanisms formation involved in this complex system.

Acknowledgements

This work was supported by The French National Research Agency (ANR) Gameco

References

1. E. Furlani, G. Tonello, E. Aneggi, and S. Maschio, *Ceram. Int.*, 2013, **39**, 1257–1263.

2. D. Świerczyński, S. Libs, C. Courson, and a. Kiennemann, *Appl. Catal. B Environ.*, 2007, **74**, 211–222.

3. L. Devi, M. Craje, P. Thüne, K. J. Ptasinski, and F. J. J. G. Janssen, *Appl. Catal. A Gen.*, 2005, **294**, 68–79.

4. J. Pecho, T. J. Schildhauer, M. Sturzenegger, S. Biollaz, and A. Wokaun, *Chem. Eng. Sci.*, 2008, **63**, 2465–2476.

5. J. Corella, J. M. Toledo, and G. Molina, *Ind. Eng. Chem. Res.*, 2007, **46**, 6831–6839.

6. G. Olofsson, Z. Ye, I. Bjerle, and A. Andersson, *Ind. Eng. Chem. Res.*, 2002, **41**, 2888–2894.

7. M. Portnyagin, R. Almeev, S. Matveev, and F. Holtz, *Earth Planet. Sci. Lett.*, 2008, **272**, 541–552.

8. P. Geysermans and C. Noguera, *J. Mater. Chem.*, 2009, **19**, 7807–7821.

9. D. Swierczynski, C. Courson, L. Bedel, A. Kiennemann, and S. Vilminot, *Chem. Mater.*, 2006, **18**, 897–905.

10. S. Rapagnà, M. Virginie, K. Gallucci, C. Courson, M. Di Marcello, A. Kiennemann, and P. U. Foscolo, *Catal. Today*, 2011, **176**, 163–168.

11. H.-S. Roh, H. S. Potdar, and K.-W. Jun, *Catal. Today*, 2004, **93-95**, 39–44.

12. K. Tomishige, T. Kimura, J. Nishikawa, T. Miyazawa, and K. Kunimori, *Catal. Commun.*, 2007, **8**, 1074–1079.

13. R. Zhang, Y. Wang, and R. C. Brown, *Energy Convers. Manag.*, 2007, **48**, 68–77.

14. M. Öhman and A. Nordin, *Energy & Fuels*, 2000, **14**, 737–737.

15. S. Rapagnà, N. Jand, A. Kiennemann, and P. U. Foscolo, *Biomass and Bioenergy*, 2000, **19**, 187–197.

16. G. Hu, S. Xu, S. Li, C. Xiao, and S. Liu, *Fuel Process. Technol.*, 2006, **87**, 375–382.

17. C. Courson, E. Makaga, C. Petit, and A. Kiennemann, *Catal. Today*, 2000, **63**, 427–437.

18. R. F. Cooper and D. L. Kohlstedt, *Phys. Chem. Miner.*, 1984, **11**, 5–16.

19. E. Furlani, G. Tonello, E. Aneggi, and S. Maschio, *Ceram. Int.*, 2012, **38**, 2619–2625.

20. R. Michel, M. R. Ammar, J. Poirier, and P. Simon, *Ceram. Int.*, 2012, **39**, 5287–5294.

21. M. Tadic, V. Kusigerski, D. Markovic, I. Milosevic, and V. Spasojevic, *J. Magn. Magn. Mater.*, 2009, **321**, 12–16.

22. F. Chen, R. Shi, Y. Xue, L. Chen, and Q.-H. Wan, *J. Magn. Magn. Mater.*, 2010, **322**, 2439–2445.

23. A.-L. Morel, S. I. Nikitenko, K. Gionnet, A. Wattiaux, J. Lai-kee-him, C. Labrugere, B. Chevalier, G. Deleris, C. Petibois, A. Brisson, and M. Simonoff, *ACS Nano*, 2008, **2**, 847–856.

24. Y. El Mendili, a Abdelouas, and J.-F. Bardeau, *Phys. Chem. Chem. Phys.*, 2013, **15**, 9197–204.

25. Z. H. Zhou, J. Wang, X. Liu, and H. S. O. Chan, *J. Mater. Chem.*, 2001, **11**, 1704–1709.

26. Y. El Mendili, J. Bardeau, N. Randrianantoandro, F. Grasset, and J. Greneche, *J. Phys. Chem. C*, 2012, **116**, 23785–23792.

27. M. Fonin, R. Pentcheva, Y. S. Dedkov, M. Sperlich, D. V. Vyalikh, M. Scheffler, U. Rüdiger, and G. Güntherodt, *Phys. Rev. B*, 2005, **72**, 104436.

28. S. V Ovsyannikov, V. V Shchennikov, S. Todo, and Y. Uwatoko, *J. Phys. Condens. Matter*, 2008, **20**, 172201 –172206.

29. P. Gay and R. W. Lemaitre, *Am. Mineral.*, 1961, **46**, 92–111.

30. J.-P. Clément, M. Caroff, P. Dudoignon, P. Launeau, M. Bohn, J. Cotten, S. Blais, and G. Guille, *Lithos*, 2007, **96**, 524–542.

Figure captions

Fig. 1. *Ex situ* X-ray diffractograms of olivine: (a) natural olivine, calcined olivine at (b) 1400°C-4h, and (c) 1400°C-115h. The insert shows the increase of proto-enstatite from 4h to 115h residence time

Fig. 2. *In situ* X-ray diffractograms of olivine: (a) 50°C, (b) 550°C, (c) 1050°C, (d) 1225°C and (e) 1400°C

Fig. 3. Reflected light micrographs using bright (BF) and dark field (DF) modes of calcined olivine grains at 1400°C - 4h, with Raman spectra (a and b) - forsterite, (c) magnetite direct spinel, (d) magnetite inverse spinel, (e) enstatite and (f) hematite

Fig. 4. (Upper hand corner) Bright field micrograph of calcined olivine grains at 1400°C – 4h and Raman map scores showing the spatial distribution of the various phases over the rectangle defined in the optical micrograph; [(a) forsterite, (b) enstatite, (c) hematite, (d) magnetite direct spinel, and (e) magnetite inverse spinel]

Fig. 5. (upper part) Dark and bright field micrographs of calcined olivine grains at 1400°C – 115h and Raman map scores showing the spatial distribution of the various phases over the rectangle defined in the optical micrograph [(a) forsterite, (b) enstatite, (c) magnetite direct spinel, and (d) magnetite inverse spinel]

Fig. 6. The various stages describing the mechanism for the phase transformation and the migration of the various oxides from olivine particles toward the surface at high temperature

Figure 1

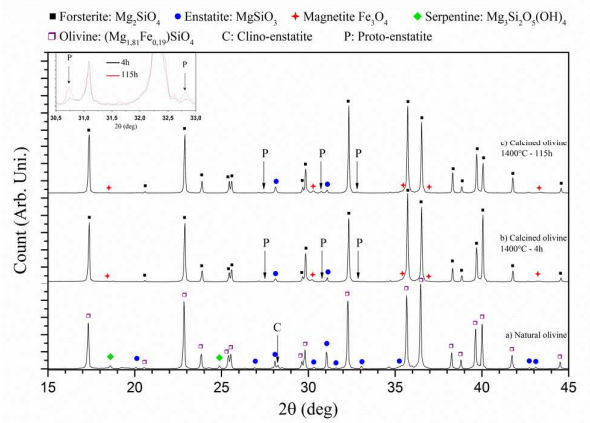

Fig. 1. *Ex situ* X-ray diffractograms of olivine: (a) natural olivine, calcined olivine at (b) 1400°C-4h, and (c) 1400°C-115h. The insert shows the increase of proto-enstatite from 4h to 115h residence time

Figure 2

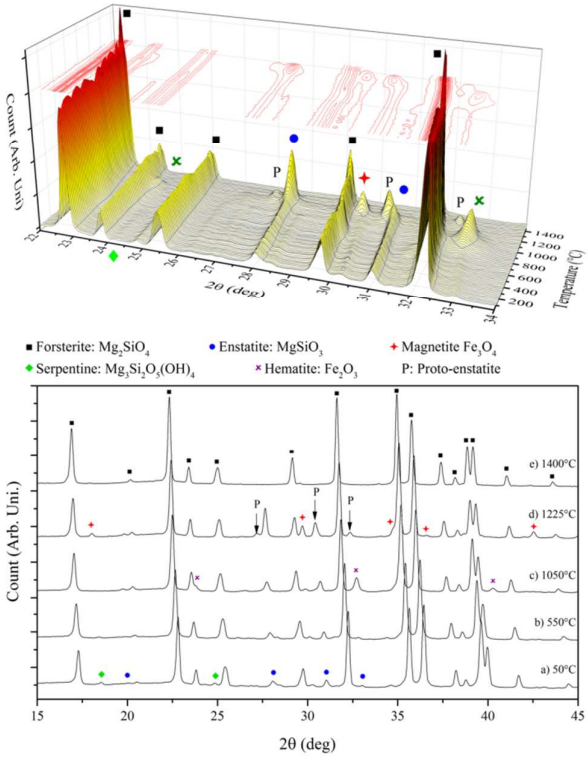

Fig. 2. *In situ* X-ray diffractograms of olivine: (a) 50°C, (b) 550°C, (c) 1050°C, (d) 1225°C and (e) 1400°C

Figure 3

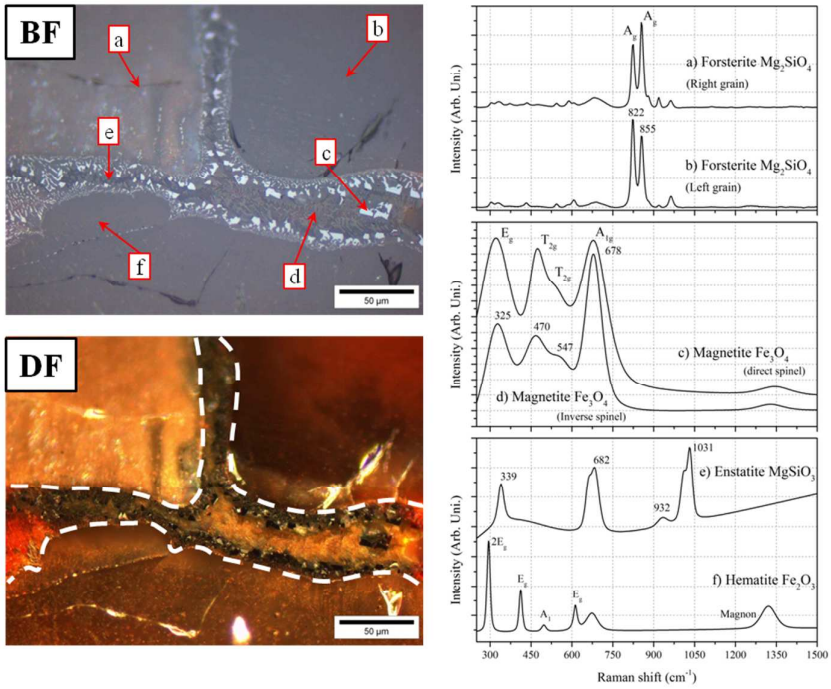

Fig. 3. Reflected light micrographs using bright (BF) and dark field (DF) modes of calcined olivine grains at 1400°C - 4h, with Raman spectra (a and b) - forsterite, (c) magnetite direct spinel, (d) magnetite inverse spinel, (e) enstatite and (f) hematite

Figure 4

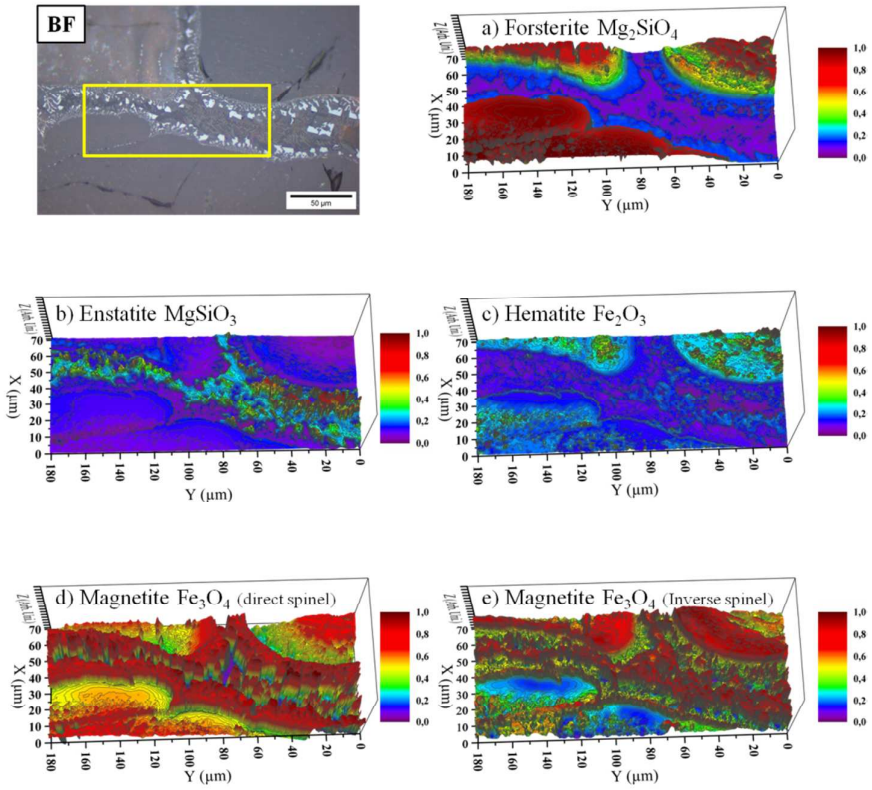

Fig. 4. (Upper hand corner) Bright field micrograph of calcined olivine grains at 1400°C – 4h and Raman map scores showing the spatial distribution of the various phases over the rectangle defined in the optical micrograph; [(a) forsterite, (b) enstatite, (c) hematite, (d) magnetite direct spinel, and (e) magnetite inverse spinel]

Figure 5

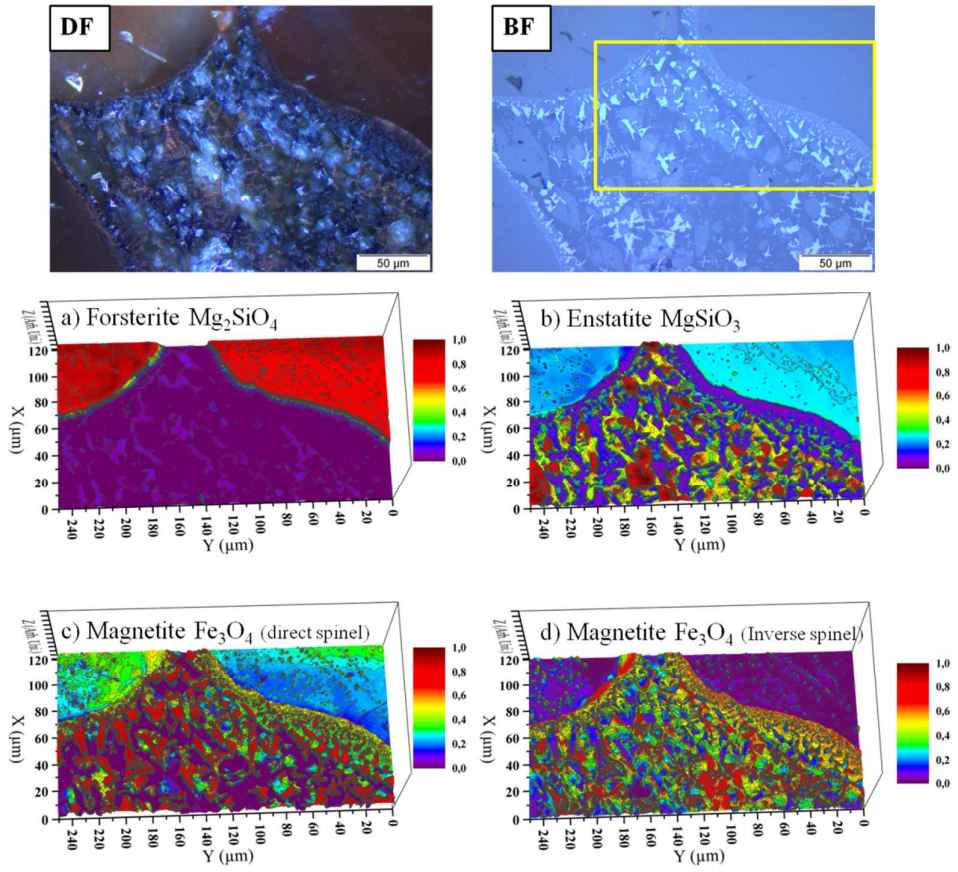

Fig. 5. (upper part) Dark and bright field micrographs of calcined olivine grains at 1400°C – 115h and Raman map scores showing the spatial distribution of the various phases over the rectangle defined in the optical micrograph [(a) forsterite, (b) enstatite, (c) magnetite direct spinel, and (d) magnetite inverse spinel]

Figure 6

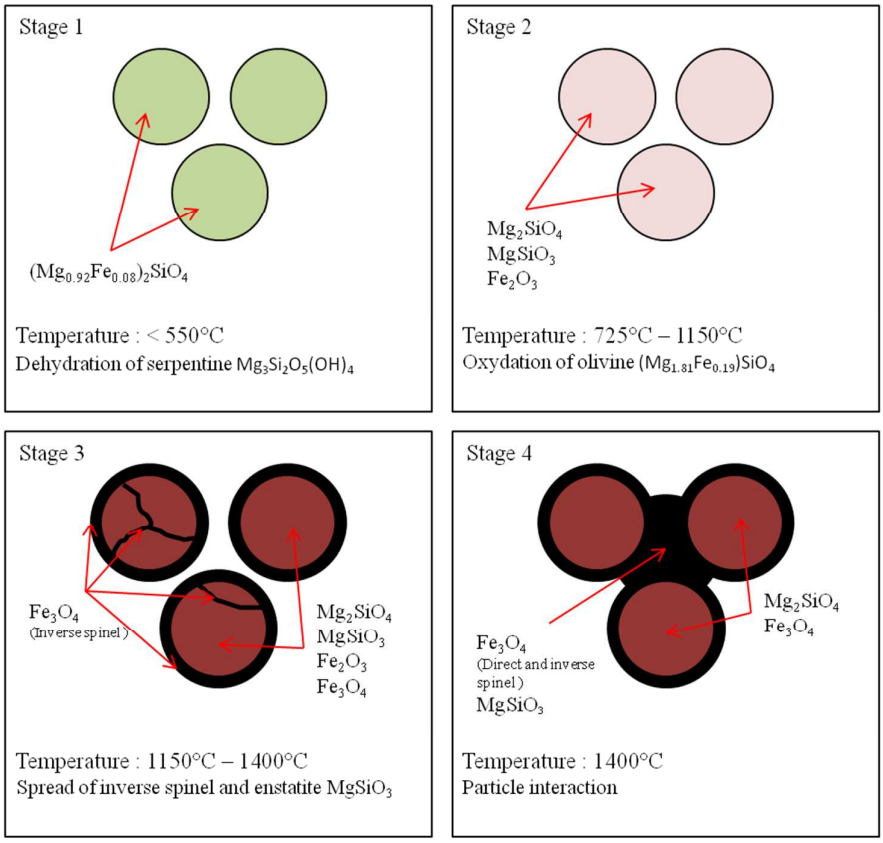

Fig. 6. The various stages describing the mechanism for the phase transformation and the migration of the various oxides from olivine particles toward the surface at high temperature